Journal of Molecular Catalysis A: Chemical 321 (2010) 101–109

Contents lists available at ScienceDirect

Journal of Molecular Catalysis A: Chemical

journal homepage: www.elsevier.com/locate/molcata

Adsorption kinetics and dynamics of CO on silica supported Au nanoclusters—Utilizing physical vapor deposition and electron beam lithography

E. Kadossov[a], S. Cabrini[b], U. Burghaus[a,*]

[a] Department of Chemistry, Biochemistry, and Molecular Biology, North Dakota State University, Fargo, ND 58105, USA
[b] Nanofabrication Facility, Molecular Foundry, LBNL, Berkeley, CA 94720, USA

ARTICLE INFO

Article history:
Received 12 November 2009
Received in revised form 3 January 2010
Accepted 4 February 2010
Available online 11 February 2010

Keywords:
Surface science
Experimental
Heterogeneous catalysis
Molecular beam scattering
Kinetics

ABSTRACT

The adsorption kinetics and dynamics of CO on silica supported Au clusters have been studied by thermal desorption spectroscopy (TDS) and molecular beam scattering. Physical vapor deposition (PVD) and electron beam lithography (EBL) have been used to fabricate the samples. According to our prior study (Kadossov et al., in press [49]), a maximum in the initial adsorption probability, S_0, occurs for 3 nm Au clusters. Therefore, in the present study, we have focused on this cluster size for PVD samples. In addition, 12 nm EBL Au clusters have been studied. This is presently one of the smallest achievable cluster sizes using EBL for macroscopic samples. Auger electron spectroscopy and scanning electron microscopy have been used to further characterize the samples. TDS revealed well-known features for PVD samples; i.e., two peaks assigned to CO adsorption on different defect sites were present. Interestingly, TDS data of EBL samples were dominated solely by one CO desorption peak. The initial adsorption probability of CO, S_0, decreased as a function of impact energy, E_i, and adsorption temperature, T_s, for both samples, which is consistent with non-activated molecular adsorption. The coverage dependence of the adsorption probability and S_0 are discussed in the framework of the capture zone model.

1. Introduction

The adsorption of CO on gold clusters has been studied extensively in the gas phase [1] and for Au clusters supported on metal oxide single crystals/thin films (model catalysts) [2–4], metal single crystals (pristine [2], defected [3], stepped [4]), HOPG [5], zeolites [6], and TiO_2 powders [7–10] as well as by theoretical techniques [3,11–15]. However, most experimental studies about the nanogold system apply kinetics and spectroscopic techniques (see, e.g., the reviews in Refs. [16–25]). For studies on Au single crystals see, e.g., Refs. [26–31]. Molecular beam scattering projects have focused on the CO oxidation reaction [32–35], rather than on the CO adsorption dynamics (gas-surface energy transfer processes) [36]. We are not aware of detailed molecular beam scattering data with CO on a nanogold system. In addition to the goal to reveal mechanistic details [16,18] of the reactivity of the nanogold system, the continuing interest in Au cluster systems is motivated by the importance of the low temperature CO oxidation reaction [22,23,37]. The adsorption of CO is the first elementary step in this bimolecular surface reaction. Therefore, a characterization of the kinetics and dynamics of CO adsorption onto Au clusters is pertinent for obtaining a mechanistic understanding of the CO oxidation and related surface reactions. In the majority of studies, the Au clusters are formed by different versions of the physical vapor deposition (PVD) technique. In this study, in addition to PVD, electron beam lithography (EBL) is utilized. Kinetics (TDS – thermal desorption spectroscopy) and dynamics data (molecular beam scattering) characterizing CO adsorption are discussed below. The samples have further been characterized using electron microscopy (SEM) and Auger electron spectroscopy (AES).

2. Experimental procedures

The measurements have been conducted by a home-built, triply-differentially pumped molecular beam system [38]. The supersonic beam is attached to a UHV (ultra-high vacuum) scattering chamber, which includes an Auger electron spectroscopy system (AES), a sputter gun, an electron beam metal evaporator, and a commercial atomic hydrogen doser. The impact energy, E_i, of the CO molecules could be varied within 0.1–0.98 eV by seeding 3% CO in He, combined with a variation of the nozzle temperature between 300 and 750 K. The adsorption probabilities for CO have been precisely (±0.02) determined by collecting adsorption tran-

* Corresponding author. Tel.: +1 7012319742; fax: +1 701 231 8831.
E-mail address: uwe.burghaus@ndsu.edu (U. Burghaus).
URL: http://www.chem.ndsu.nodak.edu (U. Burghaus).

1381-1169/$ – see front matter © 2010 Elsevier B.V. All rights reserved.
doi:10.1016/j.molcata.2010.02.009

sients (CO pressure vs. exposure time curves) applying the King and Wells [39] method.

The TDS (thermal desorption spectroscopy) set-up, which uses a mass spectrometer in the scattering chamber that is equipped with an aperture, is detailed in Ref. [40]. A combination of liquid N_2 cooling and He gas bubbled through the liquid N_2 allows the sample temperature, T_s, to be dropped down to ~93 K. The reading of the thermocouple has been calibrated *in situ* by TDS measurements of alkanes. A heating rate of 2 K/s has been used for TDS. All exposures for the TDS experiments are given in Langmuir units (1 L = 1 s at 1×10^{-6} mbar).

Scanning electron microscopy images have been collected with a Zeiss Ultra 60 (equipped with a Field Emission Gun) at the nanofabrication lab at Molecular Foundry (Lawrence Berkeley National Laboratory). The FESEM has a nominal resolution of ~1.2 nm with 20 keV for the electron beam acceleration voltage.

The noise level of the mass spectrometer reading and the noise of the AES spectra were used to determine the uncertainties of individual measurements.

3. Presentation of the results and discussion

3.1. Further experimental details, sample fabrication, and characterization

Gold has been vapor deposited on silica (SiO_2/Si(1 1 1)) at T_s = 300 K by means of the e-beam metal evaporator; i.e., physical vapor deposition (PVD) has been used. In addition, electron beam lithography (EBL) has been utilized (at Molecular Foundry, Berkeley) to fabricate model nano-array catalysts (MNAC) [41–43]. The details of the sample fabrication and cleaning are described in the following.

3.1.1. Support cleaning for PVD samples

Fig. 1 summarizes AES data detailing the cleaning procedure for the silica support used for the PVD of Au clusters. Shown are the C, O, and Si regions of the AES spectra. Panel A depicts the effect of sputtering and panels B/C the effect of oxygen annealing. (The AES curves for $\chi_{O_2} = 0$ min in Fig. 1B/C correspond to the sputtered but not annealed surface.) Briefly, sputtering the silica support (2 keV, 5×10^{-5} mbar Ar, 2 μA sample current, χ_{Ar} = 4 h total) not only removes carbon contaminants, but also reduces silica (SiO_2) to silicon. While sputtering the surface, the C AES line intensity decreases (Fig. 1A) as well as the O-AES and Si^{4+} TDS peak intensities are very small (see $\chi_{O_2} = 0$ min curves in Fig. 1B and C). The appearance of the Si^0 AES line indicates formation of silicon. Therefore, the support has been annealed in oxygen (1×10^{-5} mbar O_2, 1000–1200 K, $\chi_{O_2} = 50$ min total), which restores the oxidic surface of the wafer. After oxygen annealing, the Si^{4+} AES peaks are evident (Fig. 1C), the Si^0 AES peak intensity drops close to the detection limit (Fig. 1C), and the O-AES intensity increases (Fig. 1B). The AES curves finally obtained are consistent with data given in Ref. [44]. Please note that the modulation voltage of the lock-in amplifier has been reduced from a typical 10 V to 2 V when recording the Si AES features, which were otherwise buried under the secondary electron background, using a standard retarding field AES system. The smaller modulation voltage certainly also improves the energy resolution.

3.1.2. PVD samples – estimate of Au coverage and determining the growth mode of Au on silica

The inset of Fig. 2 depicts the gold region of the AES spectra for different deposition times, χ_{Au}, of Au (PVD sample). The main panel depicts the Au(69 eV) AES peak intensity as a function of χ_{Au}. These data provide indications for the growth mode of Au on silica and allow for an Au coverage estimate for the PVD sample.

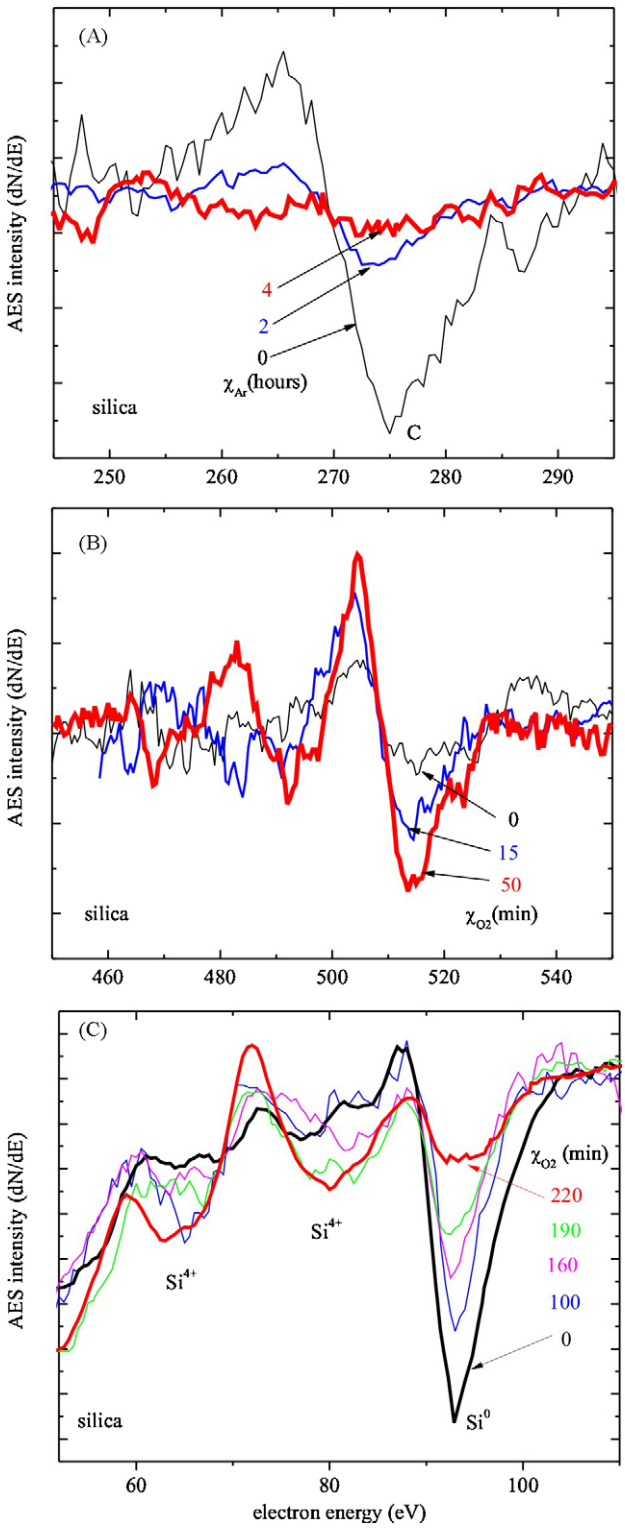

Fig. 1. AES characterization of the cleaning of the silica support. (A) Effect of sputtering (Ar^+, $p(Ar^+) = 5 \times 10^{-5}$ mbar, U = 2 keV) on the AES carbon region; (B) AES oxygen and (C) silicon regions while annealing the surface in molecular oxygen at 1000–1200 K (1×10^{-5} mbar).

According to prior STM (scanning tunneling microscopy) studies, the Au growth on silica [45,46] also can be described by the standard model commonly obeyed by model catalysts (metals-on-metal oxides) [47,48]. At small Au coverages, Θ_{Au}, a quasi-two-dimensional (2D) growth of Au clusters is present, while very large exposures lead to three-dimensional (3D) Au cluster

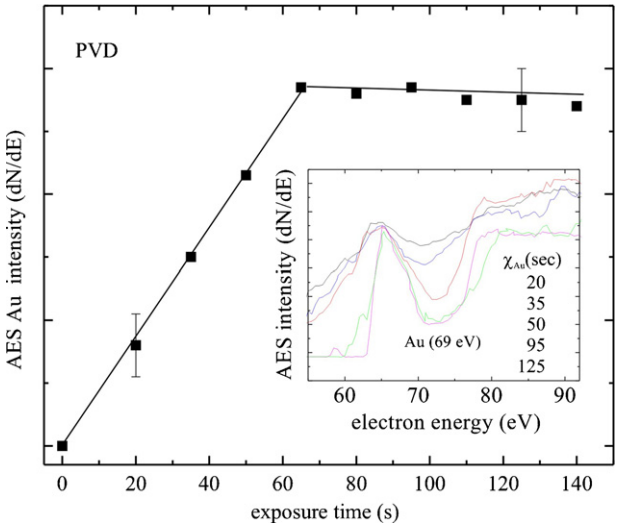

Fig. 2. Au AES intensity as a function of Au deposition time on the silica support. The inset shows the AES Au region.

growth. Furthermore, the 2D growth phase consists of two regions. At very small deposition times ($\chi_{Au} \leq 10$ s), the cluster density increases rapidly with χ_{Au}, while keeping the cluster size relatively unchanged (nucleation stage). Depositing more Au after the nucleation stage leads to an increase in the cluster size, while keeping the particle density essentially constant.

The AES results are consistent with this cluster growth model. The slope of the Au AES peak intensity vs. χ_{Au} curve decreases (Fig. 2) due to screening of the 1st layer of Au atoms (forming the 2D clusters) by the 2nd layer, as the 3D clusters start to form. Therefore, the slope change at $\chi_{Au} = 60$ s corresponds to the 2D → 3D transition and may be used to calibrate χ_{Au} in equivalent MLs. Here one equivalent ML corresponds to the start of the 3D growth regime, which corresponds, according to the STM data [45,46], to a nominal Au coverage of 18%. (A nominal Au coverage of 1 ML would correspond to a closed, and one atom thick, Au layer on the support.) For all of the CO adsorption data discussed below, which were obtained for Au exposure by PVD, χ_{Au} has been set to 10 s. Experiments where χ_{Au} has been varied are presented elsewhere [49]. According to a statistical analysis of scanning electron microscopy images of this sample (see Fig. 3A and B), $\chi_{Au} = 10$ s corresponds to ~3 nm Au clusters, a cluster density of 5×10^{-11} cm^{-2}, and a nominal Au coverage of 4%. The cluster size distribution is narrow (3 ± 2 nm). This coverage corresponds to the final stage of the nucleation regime, using an Au deposition time just before the Au clusters start to grow in size. Here, the largest dispersion (density) of small Au clusters is obtained. Importantly, the legendary reactivity enhancement for the CO oxidation reaction has been reported for 2–3 nm Au clusters [22] and the initial adsorption probability for CO, S_0, reached a maximum for this Au cluster size as determined earlier (see Ref. [49] for details). Therefore, this particular Au cluster morphology has been studied here in detail.

3.1.3. EBL samples – fabrication of model nano-array catalysts

In addition to using PVD, model nano-array catalysts have been studied [41–43] utilizing electron beam lithography (EBL). These systems consist of a predetermined pattern of metal clusters (see SEM images in Fig. 3C and E). Here 12 nm Au clusters, with an aspect ratio of 0.4 have been fabricated. The lattice constant (more commonly called "pitch" in lithography) amounts to 100 nm. A nano-size pattern with an overall macroscopic dimension, 5 mm × 5 mm, has been written on a (10 mm × 10 mm) silica support. Although this corresponds to a calculated Au coverage of only 1.4% ML (12 nm^2/100 nm^2), it was sufficient to collect kinetics and dynamics data, as described below. Fig. 3D shows the statistical analysis of the image in Fig. 3C. The particle size distribution is extremely narrow, i.e., (12 ± 1) nm (±8%). Please note that the SEM images have been collected after the UHV kinetics/dynamics experiments where the EBL samples have never been annealed in UHV above 400 K. Sintering is absent; however, displacement of some Au clusters is evident in some of the SEM images (not explicitly shown). Similar displacements of clusters have been seen in fresh samples and these appear to originate from the lift-off process used to fabricate the samples. At greater spatial resolution, the Au clusters are imaged as circular structures with a smooth rim (Fig. 3E). A number of studies have revealed that EBL samples are crystalline upon annealing [50,51]. However, the exact shape and crystal structure of the EBL samples used here has not been determined. The same holds true for most metal cluster systems obtained by PVD techniques. As far as we know, the model nano-array catalyst samples used here consist of the smallest EBL structures reported to date in a surface science/(catalysis) study. Much smaller structures can be made by EBL, but hardly over macroscopic distances, which is required for traditional surface chemistry experiments.

Since the concept of using EBL in surface science (/catalysis) is still rather novel [52–54], the fabrication procedure used here is briefly outlined as follows. The Vistec VB300 e-beam nanowriter (using an 100 keV electron beam) at LBNL (Lawrence Berkeley National Laboratory) allows for control of the pattern with an accuracy better than 1 nm and a resolution better than 10 nm; the theoretical spot size limit amounts to ~4 nm. A high resolution pattern can be written on a large area (5 mm × 5 mm) within 5–8 h. A 50 nm layer of an electron beam resist (ZEP 520A) was deposited on the silica substrate prior to electron beam exposure. After the exposure, the sample was developed (in amyl acetate). With a metal evaporator, a thin 3 nm layer of Au was then deposited on the patterned and 20° tilted substrate. Tilting the metal evaporator reduces the spot size further. The metal deposited on the surface forms initially small dots of variable size. Annealing the sample at 500 K sinters all of the small dots into a single cluster. The result is an extremely narrow particle size distribution and a patterned surface (Fig. 3C).

Considering the silica system, the reactivity of the Au clusters is determined to a large extent by two parameters: the cluster size (determining the number of catalytically active sites) and the dispersion (cluster density) [49]. In principle, both parameters can be varied and controlled independently in the nm size range, using EBL. Unfortunately, the number of model nano-array catalysts available for this study was very limited; i.e., data solely for 12 nm Au clusters (pitch 100 nm) are described below. Experiments with other metal clusters, where the smallest cluster size may not be too critical, are underway in our lab. However, nanogold can be considered as one of the most important prototype systems for model catalysts.

3.1.4. EBL samples – cleaning of model nano-array catalysts

Cleaning of EBL metal cluster systems is not a trivial matter, as discussed by other groups before [55,56], since standard techniques such as sputtering can easily destroy the sample's morphology. Chemical procedures may change the composition of the system and are typically rather inefficient at UHV conditions. However, the inertness of Au allows carbon contaminants to be cleaned off within a reasonable time by annealing the sample in a flux of atomic hydrogen, χ_H. AES data illustrating the progress of the cleaning procedure are shown in Fig. 4. As is evident, the Au clusters are atomically cleaned and their morphology is preserved, as already described above (see Fig. 3C/E). Annealing the sample in molecular oxygen or NO_2 was inefficient and atomic oxygen dosers are much more

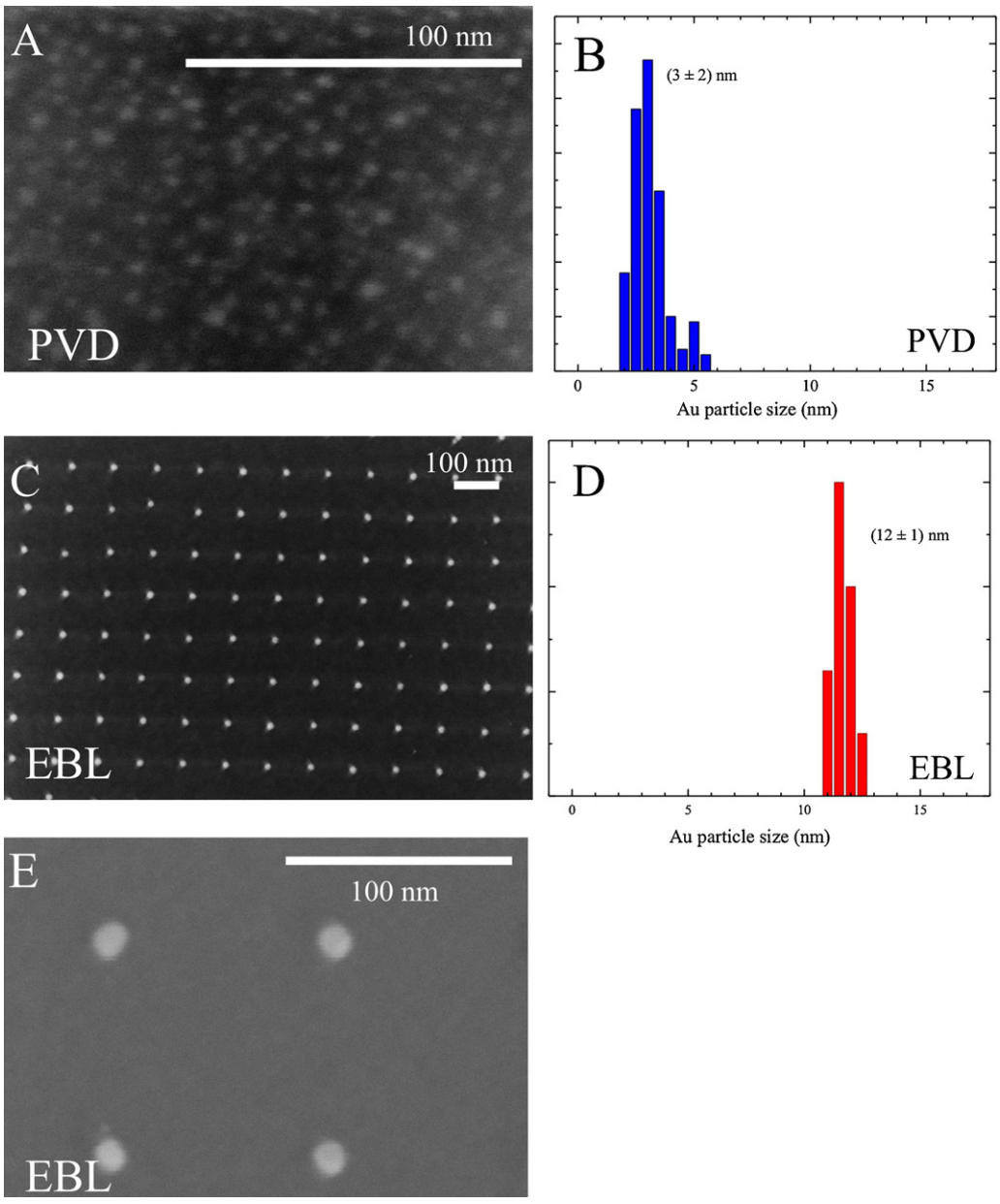

Fig. 3. (A, C, and E) Scanning electron microscopy images of PVD and EBL samples (as indicated) as well as (B and D) their statistical analysis.

complex (i.e., expensive) than an atomic hydrogen doser. A simple (home-built) W-filament doser can lead to W-contamination of the sample, particularly when using oxygen.

3.2. Adsorption kinetics of CO

CO TDS data are summarized in Fig. 5. Following a traditional outline, the data are described first, followed by a detailed discussion of the results in context with what is known from the literature including data on Au single crystals.

3.2.1. Results

Fig. 5A depicts CO TDS runs for a clean silica support as a function of CO exposure, χ_{CO}. Consistent with the literature data [57], a weak TDS feature at about 110 K is seen, which originates from the silica support (Si peak). However, at 93 K, the uptake of CO on the support is very small. The integrated intensity of the CO TDS silica feature amounts to less than 10% of the CO TDS signal detected for the Au cluster system (for 8 L CO exposure). Additionally, CO adsorption transients recorded using the molecular beam system show (at 93 K) an almost perfect square shaped (beam) profile; i.e., the CO coverage on the silica support is very small. Although the mass spectrometer has a cone shaped aperture and is placed one mm in front of the surface, the spike in the TDS data at 93 K appears to originate from the sample heating filament (labeled as the F peak).

Fig. 5B shows CO TDS data for χ_{Au} = 10 s Au deposition (3 nm Au clusters, PVD sample) as a function of CO exposure, χ_{CO}. The TDS curves consist of two main features at 150–170 K and 250 K, which are labeled as α and β peaks. While increasing the CO exposure, these peaks appear in the order of their desorption temperature (β → α), as expected. A minor low temperature shoulder at ~110 K is also evident and originates from the silica support.

Interestingly, for the EBL samples, the TDS curves are dominated by a single feature at about 175 K (see Fig. 5C), which appears to coincide approximately with the position of the α TDS peak of the PVD samples. This conclusion becomes more evident after subtract-

Table 1
Kinetics parameters for CO adsorption on supported Au clusters, silica, and Au single crystals. The binding energies, E_d, were calculated using a Redhead analysis and assuming a 1st order pre-exponential factor of 1×10^{13}/s.

System	CO TDS peak positions in K		E_d in kJ/mol		Ref.
Clean supports					
SiO_2/Si(1 1 1)	100–115		24-29		This work
SiO_2/Si(1 0 0)	105		26		[57]
Ar+ sputtered Au(1 1 1)	145, 185		44, 54		[3]
Au(1 1 1)	No adsorption at 110 K		<27		[3]
Au(1 1 0)–(1 × 2)	Multiple peaks below 70 K, wide feature up to 150 K		8.3, 9.2, 13, 16, 35		[2]
Au(3 1 0), Au(3 2 1)	100, 120, 180		24–46		[75]
Supported Au nanoclusters					
SiO_2/Si(1 1 1)-PVD	150–170	250	44	65	This work
SiO_2/Si(1 1 1)-EBL	175	–	42	–	This work
SiO_2/Si (1 0 0)	113	240	28	60	[57]
FeO (1 1 1)	130	200	32	50	[16]
Fe_3O_4 (1 1 1)	120	180–250	29	45–63	[73]
Al_2O_3/NiAl(1 1 0)	120	160–200	29	40–50	[73]
	105	143	31	42	[74]
TiO_2(1 1 0)	200–230	280	51–58	72	[36]
HOPG	130–145	170–185	34–38	44–48	[3,5]

ing the silica support TDS features (Fig. 5A) from the EBL sample data (see Fig. 5C). Fig. 5D depicts the background-corrected CO TDS curves for the EBL sample. Only one TDS structure is evident, which is labeled as the α peak. Table 1 summarizes all of the TDS peak temperatures and binding energies, with comparisons to literature data.

The CO TDS signal was obviously rather small for both the PVD and the EBL sample (Fig. 5). More precisely, the integrated CO TDS intensity for the PVD samples was larger by a factor of three compared to the EBL samples. Based on the SEM analysis, taking the cluster density and size into account, Θ_{Au} (nominal coverage) amounts to 4.5% and 1.4% for the PVD and EBL samples, respectively. In addition, large CO clusters are less reactive than small clusters. Thus, the intensity variations seen in the TDS data are consistent with differences in Θ_{Au} and with variations in cluster size dependent reactivity.

3.2.2. Discussion

Despite the variations in the peak positions (see Table 1) in prior studies on supported Au catalysts, two CO TDS peaks were consistently detected, similar to our data obtained for the PVD sample (Fig. 5A). IR (infrared spectroscopy) and TDS data indicated repulsive CO–CO interactions that were consistent with the TDS peaks shift to lower temperatures with increasing CO exposure also present in our data sets. Due to the small total CO coverage, the peak shifts are certainly small. The high temperature β TDS peak is preferentially occupied at low CO exposures (Fig. 5B), as thermodynamically expected. On defect "free" and flat gold surfaces, no CO desorption is seen (for adsorption temperatures of 110 K), whereas on Au surfaces with strong defects, both α and β TDS peaks are present [3] (see Table 1). The β TDS peak is most distinct for a system characterized by a large defect density. In most cases, these results have been assigned to CO adsorption on low-coordinated sites of Au clusters [3,11,16,58]. DFT (density functional theory) calculations indicate CO adsorption on sevenfold and sixfold coordinated sites as the energetically most favorable adsorption sites, which may be associated with CO adsorption on Au step edges and kink sites of Au clusters [3]. Adsorption on terrace sites, flat adsorbed CO, and CO bonded to bridge sites along steps has been ruled out.

Therefore, our TDS data for PVD samples (Fig. 5B) are consistent with prior work by other groups (see also Table 1). PVD techniques also have been used in all prior studies. Accordingly, we assign the α and β TDS peaks (Fig. 5B) to adsorption of CO onto different types of defect sites (e.g., kink and step sites). However, the cluster size and most likely the shape of the Au clusters of the PVD and EBL samples differ significantly. In addition, it is known from calculations (using the so-called Wulf construction) that the relative number of defect sites decreases with increasing cluster size [59]. Therefore, it is not unexpected that the shape of the TDS curves for the PVD (3 nm Au clusters) and EBL (12 nm Au clusters) samples differ. The relative fraction of defect sites should decrease with increasing cluster size [59]. Adapting the assignment of the peak positions proposed in the literature for PVD samples, the small intensity of the β TDS peak for the EBL samples would be consistent with a smaller concentration of, for example, kink sites, as compared to PVD samples.

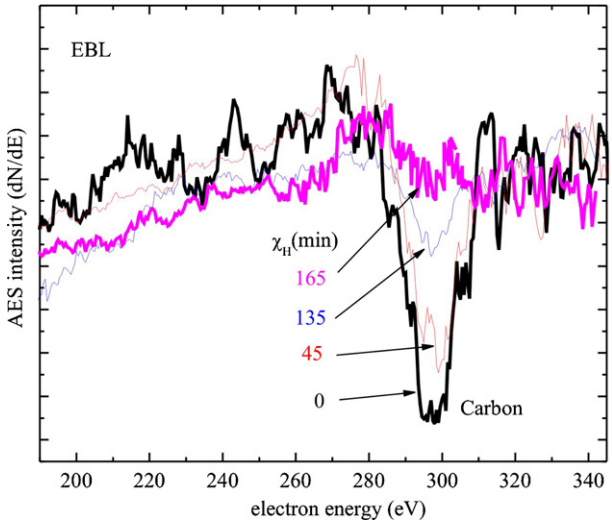

Fig. 4. AES characterization of the cleaning of the EBL samples. The carbon AES region is depicted as recorded for different annealing times in atomic hydrogen.

3.3. Adsorption dynamics of CO

Figs. 6–8 summarize the molecular beam scattering results, which map the gas-to-surface energy transfer processes (adsorption dynamics) for CO adsorption onto silica supported gold nanoparticles. Again, samples fabricated using PVD and EBL have been studied. To the best of our knowledge, no detailed UHV surface science data concerning the adsorption dynamics of CO are yet available for the nanogold system or gold single crystals. However, adsorption probabilities certainly affect surface reactions, since the concentration of reactants on the surface is related to adsorption

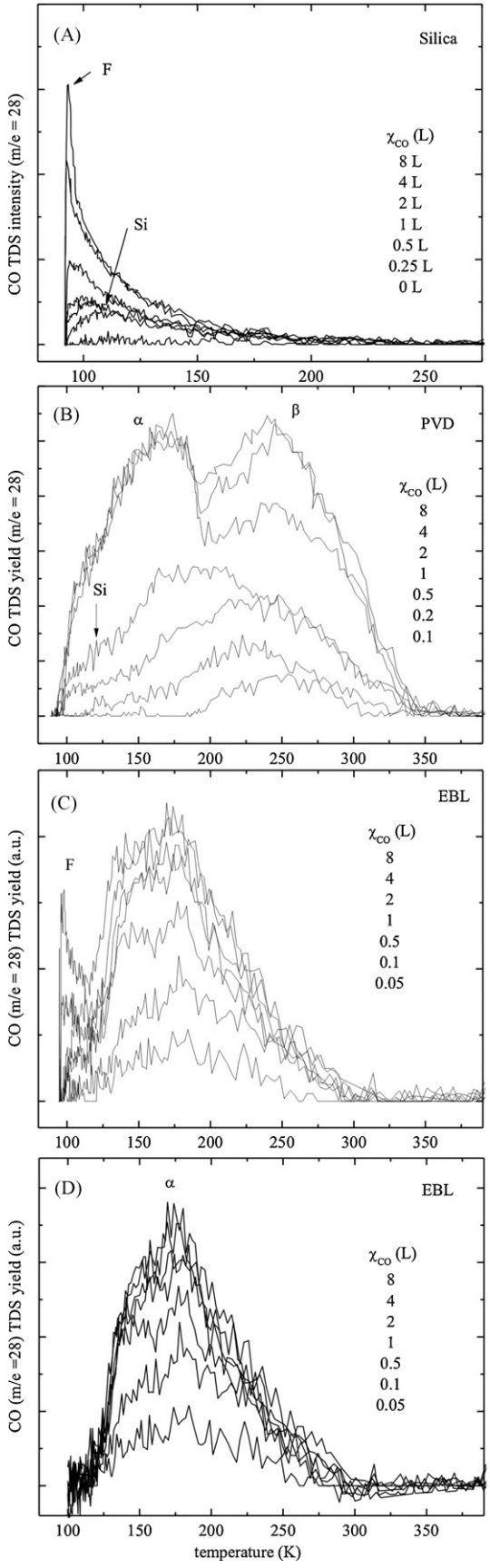

Fig. 5. TDS spectra of CO for (A) the silica support, (B) Au/SiO_2 obtained by physical vapor deposition, (C) Au/SiO_2 obtained by electron beam lithography (EBL), (D) background-corrected data for EBL sample.

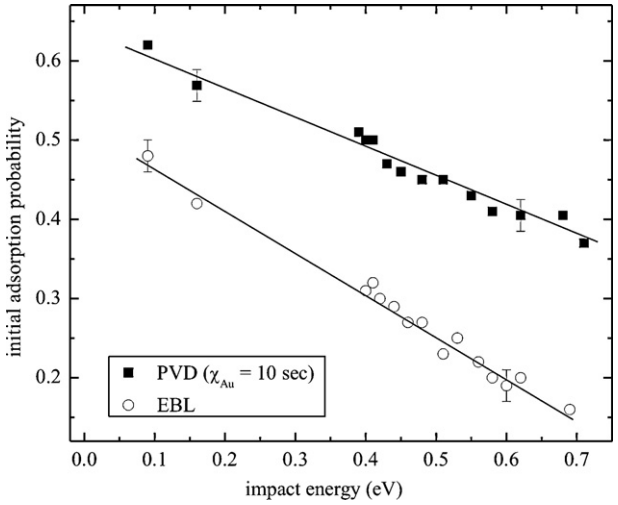

Fig. 6. Initial adsorption probability of CO for PVD and EBL Au/SiO_2 samples as a function of impact energy. Surface temperature T_s = 93 K.

probabilities. In addition, the potential energy surface of the system is mapped, providing mechanistic information.

3.3.1. Initial reactivity towards CO adsorption, S_0

3.3.1.1. Effect of impact energy. The initial adsorption probability, S_0, as a function of the impact energy of CO, is depicted in Fig. 6. Surface reactions often run most efficiently at rather great surface temperatures (e.g., surmounting activation barriers), where surface concentrations are small. In this case, the adsorption probability in the limit of zero coverage, S_0, can be an important and realistic parameter.

S_0 decreases with increasing impact energy, E_i, (Fig. 6) which indicates molecular and non-activated adsorption, as commonly seen for CO adsorption on metal single crystals (see, e.g., Refs. [60,61]), and which is consistent with the TDS data described above. In this case, the efficiency of the gas-surface energy transfer decreases with increasing E_i; i.e., S_0 decreases with E_i. Large values of E_i correspond to a large velocity of the gas-phase species and a small interaction time with the surface, which makes the energy transfer increasingly more inefficient as E_i increases. In contrast,

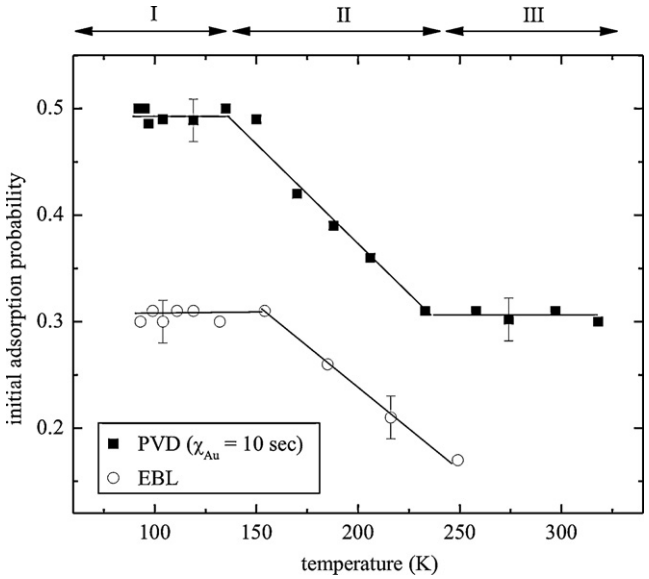

Fig. 7. Initial adsorption probability of CO for PVD and EBL Au/SiO_2 samples as a function of surface temperature. CO beam impact energy 0.39 eV.

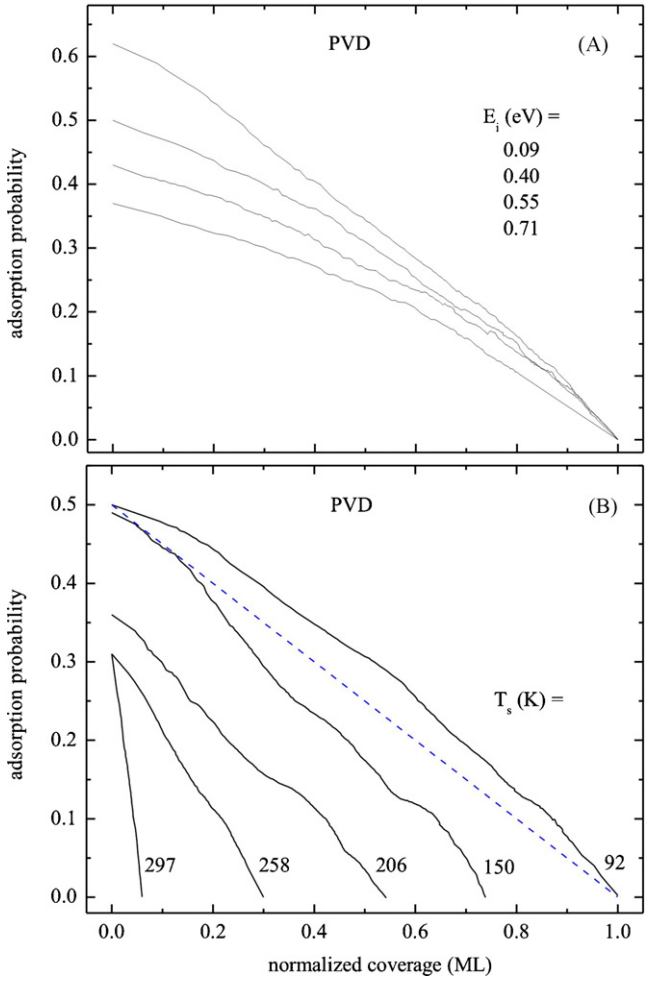

Fig. 8. Coverage dependence of adsorption probability $S(\Theta)$ of CO on vapor-deposited Au clusters at different (A) CO beam impact energies, (B) surface temperatures. Au deposition time 10 s.

for an activated adsorption, S_0 would be expected to increase with E_i above a given threshold energy [62]. S_0 can be parameterized as $S_0(\text{PVD}) = 0.64–0.38\ E_i$ and $S_0(\text{EBL}) = 0.52–0.53E_i$ (with E_i in eV). Extrapolating S_0 to thermal impact energies ($E_i = 0.04$ eV), for example, obtained in a backfilling experiment, results in $S_0 = 0.62$ and 0.50 for PVD and EBL samples.

Although the slopes of the S_0 vs. E_i curves are approximately identical for both samples, S_0 for the PVD sample is larger than for the EBL sample. According to our prior work, this simply reflects the effect of the Au cluster size [49]. S_0 reached a maximum for 3 nm Au clusters [49] and decreased for smaller and larger particles. The EBL sample size amounts to 12 nm and the PVD sample also has a rather narrow Au cluster size distribution, with a maximum at 3 nm for $\chi_{Au} = 10$ s. Therefore, $S_0(\text{PVD}) > S_0(\text{EBL})$. In a prior study [49], we attributed this effect to a maximum of active sites for CO adsorption present for 3 nm clusters. A deposition time of $\chi_{Au} = 10$ s corresponds to the end of the Au nucleation phase on the silica support. For larger deposition times, the clusters start to grow. Large Au clusters are less reactive than 3 nm clusters. For Au deposition times smaller than 10 s, not all nucleation sites are decorated with Au clusters. Therefore, $\chi_{Au} = 10$ (or 3 nm Au clusters) appears to be the optimum, resulting in the largest number of small and catalytically active Au clusters on the silica support. Thus, $S_0^{\text{PVD}}(3\text{ nm}) > S_0^{\text{EBL}}(12\text{ nm})$.

3.3.1.2. Effect of surface temperature. As evident from Fig. 7, the $S_0(T_s)$ curves consist of three segments, as indicated. S_0 is initially constant and then decreases with increasing adsorption temperature, until S_0 levels out at large T_s. For molecular and non-activated adsorption, S_0 would be independent of surface temperature, T_s, up to the temperature where the thermal desorption of the molecules becomes significant (see, e.g., Ref. [63]). At that temperature, S_0 would also decrease for molecular adsorption; however, this is a simple kinetic effect (desorption rate competes with adsorption rate) and does not reflect the adsorption dynamics (see, e.g., Ref. [64]). However, according to the TDS data shown in Fig. 5, the decrease in S_0 seen here for $T_s > 150$ K (Section 2) cannot be related to the thermal desorption of CO, which starts only above 250–300 K.

However, $S_0(T_s)$ curves similar to those depicted in Fig. 7 are commonly observed for supported cluster systems (see, e.g., Ref. [48]). The decrease in S_0 with T_s is again a kinetic effect, rather than a dynamic effect, and is typically explained in the framework of the so-called capture zone model (see, e.g., Refs. [48,65–70]). Accordingly, CO molecules are trapped in a precursor state before they adsorb/desorb. Thus, the molecules diffuse along the support, then either revert to the gas phase or adsorb onto the metal clusters, as the high binding energy sites. The probability for the CO molecules to be captured by the Au clusters depends on the lifetime of this precursor state and on the hopping (diffusion) time. These characteristic time intervals are determined by the binding energy, E_d, and the activation energy for diffusion, E_{diff}. Thus, the decrease seen in S_0 with T_s (Section 2) is a kinetic effect and reflects the interplay of the surface residence time and diffusion (hopping) time. Both the desorption rate and diffusion rate increase with temperature; i.e., the surface residence time and hopping time decrease with T_s. However, since $E_d \gg E_{diff}$, the capture zone decreases with increasing T_s. Hence, the efficiency with which a CO molecule is captured by the Au clusters decreases with T_s, as is observed: S_0 decreases with T_s (see Fig. 7, Section 2). At low temperatures, the capture zones around the Au clusters are large and eventually overlap. Therefore, S_0 is independent of T_s at low adsorption temperatures (Section 1) and here, S_0 reflects the probability for molecular adsorption. At large T_s (Section 3), the capture zones are negligibly small (very short surface residence time) and the adsorption scenario may be dominated by direct adsorption events (without a precursor) on the Au clusters, an explanation also invoked in Ref. [71]. However, regarding the small Au coverage, S_0 is still fairly large, even at large temperatures. Although at high temperatures the CO coverage is negligibly small (which rules out the effect of extrinsic precursor states), an influence of an intrinsic precursor cannot be ruled out (see also next section). The latter would lead to an enhancement of S_0.

Considering the differences in S_0 seen for PVD and EBL samples, it is evident from Fig. 7 that $S_0^{\text{PVD}}(T_s) > S_0^{\text{EBL}}(T_s)$. The capture zone is certainly larger for larger clusters, which appears to contrast with the experimental results. One may note again, however, that the variations in the absolute value of S_0, for the two different samples, is also caused by variations in the number of active adsorption sites on the Au clusters (see discussion above). $S_0^{\text{PVD}}(T_s) > S_0^{\text{EBL}}(T_s)$ since the 3 nm PVD cluster consists of many more active adsorption sites than 12 nm EBL gold clusters.

3.3.2. Coverage dependent adsorption dynamics

In Fig. 8, the CO coverage, Θ, dependence of the adsorption probability, $S(\Theta)$, is shown for the PVD sample. The CO coverage for the EBL samples was too small to properly determine $S(\Theta)$. The top panel depicts the effect of the impact energy on $S(\Theta)$ and the bottom panel summarizes $S(\Theta)$ data parametric in T_s. In the latter case, the saturation coverage of CO, i.e., Θ at $S(\Theta) \to 0$, has been obtained by integrating the adsorption transients and by normalizing the saturation coverage for CO to 1 ML for the lowest adsorption temperature: a common procedure [63]. This is an apparent coverage, since the CO molecules adsorb solely on the Au clusters.

For a direct adsorption, hit-and-stick mechanism S would simply decrease with $1-\Theta$, as the number of available adsorption sites (Langmuirian adsorption dynamics). A decrease of S with Θ slower than predicted by $S_0(1-\Theta)$ indicates the presence of precursor states, which would be expected in the framework of the capture zone model described above. The molecules diffuse along the support until they adsorb onto the Au clusters or desorb. However, the $S(\Theta)$ curves for the nanogold system are fairly steep, with a slope close to what would be predicted by the Langmuirian model (see the dashed line in Fig. 8B). However, we propose that this is simply the result of the small overall CO coverage, which suppresses an extrinsic (CO trapped above sites occupied by CO molecules) precursor state. The binding energies for CO on nanogold are consistent with a chemisorption (Table 1). Thus, an intrinsic precursor state (CO trapped in the physisorption well before chemisorbing onto the Au clusters) should exist, which could result in the slower decrease of S with Θ than the one expected for a direct adsorption process. Another possibility that may lead to $S(\Theta)$ curve shapes close to Langmuirian dynamics would be the effect of an Au cluster ensemble consisting of different Au cluster sizes. Smaller Au clusters saturate before large Au clusters, which could lead to a more linear decrease in S with Θ. However, the Au cluster size distribution is very narrow (see Fig. 3), which rules this effect out. Similar curve shapes have been seen for other cluster systems, such as Cu-on-ZnO (Ref. [68]) or Rh-on-saphire (Ref. [72]). The explanations proposed for these other systems, such as non-thermal precursor states or defects on the support (well-known for ZnO), which may lead to uncommon diffusion kinetics, appear unlikely for silica supports and gold nanoclusters. Therefore, we attribute the nearly Langmuirian shape of $S(\Theta)$ to the small CO coverage and possibly to an intrinsic precursor state.

4. Summary

Two different Au nanocluster systems (based on PVD – physical vapor deposition, and EBL – electron beam lithography) have been studied thoroughly, utilizing kinetic (TDS – thermal desorption spectroscopy), spectroscopic (AES – Auger electron spectroscopy), spatially resolved (SEM – scanning electron microscopy), and dynamic (molecular beam scattering) measuring techniques. Hydrogen "plasma etching" emerged as the most efficient technique in cleaning Au EBL samples, conserving their morphology. Both systems are characterized by fairly narrow Au particle size distribution, Au clusters of (3 ± 2) nm (PVD) and (12 ± 1) nm (EBL) have been studied. The 3 nm cluster corresponds to a morphology with the largest initial adsorption probability, S_0, for CO [49]. CO TDS for PVD samples reveals the two well-known defect peaks, commonly assigned to adsorption on kink and step sites. Interestingly, EBL TDS data consist only of one defect structure. Temperature and impact energy effects on S_0 are consistent with molecular and non-activated adsorption and were discussed in the framework of the capture zone model. S_0 as well as the coverage dependence of the adsorption probability may indicate the effect of an intrinsic precursor state.

Acknowledgments

Financial support by an NSF-CAREER award (CHE-0743932) is acknowledged by NDSU. Assistance by J. Justin at NDSU is acknowledged. Work at the Molecular Foundry (Berkeley) was supported by the U.S. Department of Energy, Office of Basic Energy Sciences through Contract No. DE-AC02-05CH11231.

References

[1] M. Neumaier, F. Weigend, O. Hampe, M.M. Kappes, J. Chem. Phys. 122 (2005) 104702.
[2] J.M. Gottfried, K.J. Schmidt, S.L.M. Schroeder, K. Christman, Surf. Sci. 536 (2003) 206.
[3] W.L. Yim, T. Nowitzki, M. Necke, H. Schnars, P. Nickut, J. Biener, M.M. Biener, V. Zielasek, K. Al-Shamery, T. Kluener, M. Baeumer, J. Phys. Chem. C 111 (2007) 445.
[4] C. Ruggiero, P. Hollins, Surf. Sci. 377–379 (1997) 583.
[5] T. Nowitzki, P. Nickut, C. Deiter, J. Wollschlaeger, K. Al-Shamery, M. Baeumer, Science 600 (2006) 3595.
[6] A.N. Pestryakov, N. Bogdanchikova, A. Simakov, I. Tuzovskaya, F. Jentoft, M. Farias, A. Diaz, Surf. Sci. 601 (2007) 3792.
[7] Y. Iizuka, H. Fujiki, N. Yamauchi, T. Chijiiwa, S. Arai, S. Tsubota, M. Haruta, Catal. Today 36 (1997) 115.
[8] S. Derrouiche, P. Gravejat, D. Bianchi, J. Am. Chem. Soc. 126 (2004) 13010.
[9] E. Roze, E. Quinet, V. Caps, D. Bianchi, J. Phys. Chem. C 113 (2009) 8194.
[10] E. Roze, P. Gravejat, E. Quinet, J.L. Rousset, D. Bianchi, J. Phys. Chem. C 113 (2009) 1037.
[11] M. Mavrikakis, P. Stoltze, J.K. Norskov, Catal. Lett. 64 (2000) 101.
[12] P. Schwerdtfeger, M. Lein, R.P. Krawczyk, C.R. Jacob, J. Chem. Phys. 128 (2008) 124302.
[13] L. Piccolo, D. Loffreda, F.J.C.S. Aires, C. Deranlot, Y. Jugnet, P. Sautet, J.C. Bertolini, Surf. Sci. 566–568 (2004) 995.
[14] Z.P. Liu, P. Hu, A. Alavi, J. Am. Chem. Soc. 124 (2002) 14770.
[15] M. Mavrikakis, B. Hammer, J.K. Norskov, Phys. Rev. Lett. 81 (1998) 2819.
[16] C. Lemire, R. Meyer, S. Shaikhutdinov, H.J. Freund, Angew. Chem. Int. Ed. 43 (2004) 118.
[17] U. Heinz, U. Landman (Eds.), Nanocatalysis (NanoScience and Technology), Springer, 2007, ISBN 978-3-540-74551-8.
[18] M. Valden, X. Lai, D.W. Goodman, Science 281 (1998) 1647.
[19] G.C. Bond, D.T. Thompson, Catal. Rev. -Sci. Eng. 41 (1999) 319.
[20] R. Burks, Chem. Eng. News 85 (2007) 87.
[21] D. Cameron, R. Holliday, D. Thompson, J. Power Sources 118 (2003) 298.
[22] M. Haruta, Catal. Today 36 (1997) 153.
[23] M. Haruta, B.S. Uphade, S. Tsubota, A. Miyamoto, Res. Chem. Intermed. 24 (1998) 329.
[24] A. Sanchez, S. Abbet, U. Heinz, W.D. Schneider, H. Häkkinen, R.N. Barnett, U. Landman, J. Phys. Chem. A 103 (1999) 9573.
[25] R. Grisel, K.J. Weststrate, A. Gluhoi, B.E. Nieuwenhuys, Gold Bull. 35 (2002) 39.
[26] J.M. Gottfried, K. Christmann, Surf. Sci. 566–568 (2004) 1112.
[27] J.M. Gottfried, K.J. Schmidt, S.L.M. Schroeder, K. Christmann, Surf. Sci. 511 (2002) 65.
[28] J.M. Gottfried, K.J. Schmidt, S.L.M. Schroeder, K. Christmann, Surf. Sci. 525 (2003) 184.
[29] J.M. Gottfried, K.J. Schmidt, S.L.M. Schroeder, K. Christmann, Surf. Sci. 525 (2003) 197.
[30] J.M. Gottfried, K.J. Schmidt, S.L.M. Schroeder, K. Christmann, Surf. Sci. 536 (2003) 206.
[31] K.F. Peters, P. Steadman, H. Isern, J. Alvarez, S. Ferrer, Surf. Sci. 467 (2000) 10.
[32] S. Lee, C. Fan, T. Wu, S.L. Anderson, J. Am. Chem. Soc. 126 (2004) 5682.
[33] T.S. Kim, J.D. Stiehl, C.T. Reeves, R.J. Meyer, C.B. Mullins, J. Am. Chem. Soc. 125 (2003) 2018.
[34] J.D. Stiehl, T.S. Kim, S.M. McClure, C.B. Mullins, J. Am. Chem. Soc. 126 (2004) 13574.
[35] J.D. Stiehl, T.S. Kim, C.T. Reeves, R.J. Meyer, C.B. Mullins, J. Phys. Chem. B 108 (2004) 7917.
[36] S. Lee, C. Fan, T. Wu, S.L. Anderson, Surf. Sci. 578 (2005) 5.
[37] T.V. Choudhary, D.W. Goodman, Top. Catal. 21 (2002) 25.
[38] J. Wang, U. Burghaus, J. Chem. Phys. 122 (2005) 044705.
[39] D.A. King, M.G. Wells, Surf. Sci. 29 (1972) 454.
[40] J. Wang, B. Hokkanen, U. Burghaus, Surf. Sci. 577 (2005) 158.
[41] F.H. Ribeiro, G.A. Somorjai, Recl. Trav. Chim. Pays-Bas 113 (1994) 419.
[42] P.W. Jacobs, F.H. Riberio, G.A. Somorjai, S.J. Wind, Catal. Lett. 37 (1996) 131.
[43] K. Wong, S. Johansson, B. Kasemo, 114 (Surface Science of Metal Oxides) Faraday Discuss. 105 (1996) 237.
[44] K. Luo, D.Y. Kim, D.W. Goodman, J. Mol. Catal. A: Chem. 167 (2001) 191.
[45] B.K. Min, W.T. Wallace, D.W. Goodman, J. Phys. Chem. B 108 (2004) 14609.
[46] W.T. Wallace, B.K. Min, D.W. Goodman, J. Mol. Catal. A: Chem. 228 (2005) 3.
[47] C.T. Campbell, Surf. Sci. Rep. 27 (1997) 1.
[48] J. Wang, U. Burghaus, J. Chem. Phys. 123 (2005) 184716.
[49] E. Kadossov, J. Justin, M. Lu, D. Rosenmann, L.E. Ocola, S. Cabrini, U. Burghaus, Chem. Phys. Lett. 483 (2009) 250.
[50] H. Iddir, V. Komanicky, S. Ogut, H. You, P. Zapol, J. Phys. Chem. C 111 (2007) 14782.
[51] R. O'Barr, S.Y. Yamamoto, S. Schultz, W. Xu, A. Scherer, J. Appl. Phys. 81 (1997) 4730.
[52] L.J. Guo, J. Phys. D: Appl. Phys. 37 (2004) R123.
[53] B.D. Gates, Q. Xu, J.C. Love, D.B. Wolfe, G.M. Whitesides, Ann. Rev. Mater. Res. 34 (2004) 339.
[54] M. Schildenberger, Y. Bonetti, M. Aeschlimann, L. Scandella, J. Gobrecht, R. Prins, Catal. Lett. 56 (1998) 1.
[55] A.S. Eppler, J. Zhu, E.A. Anderson, G.A. Somorjai, Top. Catal. 13 (2000) 33.
[56] J. Zhu, G.A. Somorjai, Nano Lett. 1 (2001) 8.
[57] E. Gross, M. Asscher, M. Lundwall, D.W. Goodman, J. Phys. Chem. C 111 (2007) 16197.
[58] L. Vattuone, L. Savio, M. Rocca, Surf. Sci. Rep. 63 (2008) 101.
[59] S. Schimpf, M. Lucas, C. Mohr, U. Rodemerck, A. Bruchner, J. Radnik, H. Hofmeister, P. Claus, Catal. Today 72 (2002) 63.

[60] U. Burghaus, J. Ding, W.H. Weinberg, J. Vac. Sci. Technol. A 16 (1998) 1010.
[61] M. Kunat, C. Boas, T. Becker, U. Burghaus, C. Wöll, Surf. Sci. 474 (2001) 114.
[62] E. Kadossov, U. Burghaus, Chem. Commun. (2008) 4073.
[63] U. Burghaus, J. Ding, W.H. Weinberg, Surf. Sci. 384 (1997) L869.
[64] J. Ding, U. Burghaus, W.H. Weinberg, Surf. Sci. 446 (2000) 46.
[65] M. Bowker, P. Stone, R. Bennett, N. Perkins, Surf. Sci. 497 (2002) 155.
[66] C.R. Henry, Surf. Sci. Rep. 31 (1998) 231.
[67] F. Rumpf, H. Poppa, M. Boudard, Langmuir 4 (1988) 722.
[68] J. Wang, E. Johnson, U. Burghaus, Chem. Phys. Lett. 410 (2005) 131.
[69] L. Piccolo, C.R. Henry, J. Mol. Catal. A: Chem. 167 (2001) 181.
[70] L. Piccolo, C.R. Henry, Surf. Sci. 452 (2000) 198.
[71] J. Libuda, H.J. Freund, Surf. Sci. Rep. 57 (2005) 157.
[72] V. Nehasil, I. Stara, V. Matolin, Surf. Sci. 377–379 (1997) 813.
[73] S. Shaikhutdinov, R. Meyer, M. Maschitzki, M. Baumer, H.-J. Freund, Catal. Lett. 86 (2003) 211.
[74] C. Winkler, A.J. Carew, S. Haq, R. Raval, Langmuir 19 (2003) 717.
[75] C.J. Weststrate, E. Lundgren, J.N. Anderson, E.D.L. Rienks, A.C. Gluhoi, J.W. Bakker, I.M.N. Groot, B.E. Nieuwenhuys, Surf. Sci. 603 (2009) 2152.